nature photonics

SUPPLEMENTARY INFORMATION

https://doi.org/10.1038/s41566-018-0139-y

In the format provided by the authors and unedited.

Giant collimated gamma-ray flashes

Alberto Benedetti, Matteo Tamburini * and Christoph H. Keitel

Max-Planck-Institut für Kernphysik, Heidelberg, Germany. *e-mail: matteo.tamburini@mpi-hd.mpg.de

Giant collimated gamma-ray flashes: Supplementary information

Alberto Benedetti[1], Matteo Tamburini[1,*], and Christoph H. Keitel[1]

[1]Max-Planck-Institut für Kernphysik, Saupfercheckweg 1, 69117 Heidelberg, Germany
[*]matteo.tamburini@mpi-hd.mpg.de

In our scheme gamma rays are generated within a solid target in the presence of strong self-generated electromagnetic fields. Thus, the photoelectric effect, Compton scattering, and electron-positron pair production might significantly affect the generated gamma-ray beam. Here we show that, for the beam and for the target parameters considered in our work, all the above-mentioned photon-target interactions are negligible for photon energies ranging from $\hbar\omega_{\text{min}} = 200$ keV up to $\hbar\omega_{\text{max}} = \gamma_b m_e c^2 + \Delta E_b = 2.5$ GeV, where $\Delta E_b \sim 0.5$ GeV has been introduced to take into account the electron beam energy spread.

In Supplementary Fig. 1 we plot the cross sections of the most important processes occurring when a photon with energy $\hbar\omega \in [1\ \text{keV}, 10\ \text{GeV}]$ travels across metallic Strontium[1] ($Z = 38$). The total cross section $\sigma_{\text{tot}}(\omega)$ (see the black line in Supplementary Fig. 1) can be employed to compute the intensity attenuation[2] $I(\omega) = I_0 \exp[-zd\sigma_{\text{tot}}(\omega)]$ when a photon beam with initial intensity I_0 has travelled across a target with thickness z and density d. In Supplementary Fig. 2 we plot the ratio $I(\omega)/I_0$ for the target width $z_{\text{max}} = 0.05$ cm and density $d_{\text{Sr}} = 2.54$ g/cm^3 considered in our work. From the inset in Supplementary Fig. 2 we see that more than 97% (99%) of the photons with energy $\hbar\omega \in [0.2, 0.5]$ MeV ($\hbar\omega \in [0.5, 10^4]$ MeV) are unaffected by the presence of the medium.

In addition, we estimate the probability for a photon to convert into an electron-positron pair in the presence of the electromagnetic field self-generated by the electron beam while crossing the target. The probability per unit time for a photon to convert into an electron-positron pair is[3]:

$$W_e = \frac{\alpha m_e^2 c^4}{6\sqrt{3}\pi\hbar^2\omega} \int_1^\infty du\ \frac{8u+1}{u^{3/2}\sqrt{u-1}}\ K_{2/3}(\xi)\ , \tag{S1}$$

where $\xi \equiv 8u/(3\chi_\gamma)$, $\chi_\gamma = (\hbar\omega/m_e c^2)(F_\perp/F_{\text{Cr}})$, $F_\perp$ is the strength of the electromagnetic field in the plane perpendicular to the photon propagation direction, and $F_{\text{Cr}} = m_e^2 c^3/|e|\hbar \approx 4.4 \times 10^{13}$ esu is the QED critical field. Since W_e in Supplementary equation (S1) is a function of the photon frequency ω, in Supplementary Fig. 3 we plot $W_e(\omega) z_{\text{max}}/c$, which is the probability for a single gamma-ray photon to create one electron-positron pair when it travels a distance $z_{\text{max}} = 0.05$ cm across an electromagnetic field with constant intensity $F_\perp = 10^9$ esu. This field strength $F_\perp$ is several times the maximum average field $\langle F_\perp^2 \rangle_{n_b}^{1/2} \approx 2 \times 10^8$ esu, that is achieved in our 3D PIC simulations, in order to account for the deviations from the mean value. Supplementary Fig. 3 shows that the electron-positron pair production probability is always smaller than 10^{-3} even for photons with $10^4\, m_e c^2$ energy, which is significantly larger than the maximal photon energy considered here $\hbar\omega_{\text{max}} = 2.5$ GeV. In fact, from the inset in Supplementary Fig. 3 (the vertical dashed line corresponds to $\hbar\omega_{\text{max}} = 2.5$ GeV), the pair production probability is $< 10^{-8}$ for photons with $\hbar\omega \leq \hbar\omega_{\text{max}} = 2.5$ GeV and, as a consequence, can be safely neglected.

In order to determine the effect of electron-atom collisions, we have also performed collisionless simulations. These simulations are in all aspects identical to those presented and discussed in our paper, including the initial conditions, but the multiple scattering routines are disabled. In Supplementary Fig. 4a and Supplementary Fig. 4b we report respectively the evolution of the electron beam number density distribution in the plane perpendicular to the beam propagation direction (xy-plane) and the evolution of the electron beam momentum distribution in the $p_z p_x$-plane for $n_b = 3 \times 10^{19}$ cm^{-3}. The left and the right column of Supplementary Fig. 4a and of Supplementary Fig. 4b display the results obtained with and without collisions, respectively. Supplementary Figs. 4a-4b show that both the electron beam dynamics and the density modulations are almost identical with and without collisions, which implies that collisions play a negligible role for our beam and target parameters. In addition, the electron-electron scattering cross section is Z^2 times smaller than the electron-atom scattering cross section, which implies that the effect of electron-electron collisions is smaller than that of electron-atom collisions, and therefore can be safely neglected.

In Supplementary Fig. 5 we show the evolution of the spatial distribution of the transverse electromagnetic field $F_\perp = \sqrt{(E_x - B_y)^2 + (E_y + B_x)^2}$ in the plane perpendicular to the electron beam propagation direction (xy-plane, the beam propagates along the z axis), for all the beam densities considered in our paper. At the beginning of the electron beam-target interaction, as the beam-target plasma instability develops, structures with size of the order of the target plasma skin depth c/ω_e appear in $F_\perp$. This initial phase corresponds to the linear regime of the electromagnetic instability and, in agreement with the instability growth rate in equation (1) of the paper, the instability develops faster with increasing beam density. In this phase the initial energy of the electron beam is gradually transferred to the electromagnetic field and consequently to the electrons of the target return current. Thus, as the beam propagates inside the target and the instability further develops and enters into its non-linear phase, the distribution of $F_\perp$ becomes more complex, because it is determined both by the electron beam density distribution and by the target density distribution, the target density being much larger than the electron beam density for all the considered cases.

The local-constant-crossed-field approximation (LCFA) is essential for the applicability of equation (8) of our paper, which gives the intensity and the energy spectrum of the radiation emitted by an electron in the presence of a background electromagnetic field. Since in all the considered cases electrons remain ultra-relativistic for the whole beam-target interaction, and the electromagnetic fields transverse to the electron propagation direction are much smaller than the QED critical field F_{Cr}, then the LCFA is applicable if each photon emission by the electrons of the beam occurs in a region (the so called formation region) which is much smaller than the region where the electromagnetic fields vary significantly[3]. Thus, it must be that $\eta = |\dot{F}|\Delta\tau/F \ll 1$, where F is the magnitude of the electromagnetic fields which accelerate the electron, $\dot{F}$ its time derivative, and $\Delta\tau$ the time the electron needs to turn by an angle $1/\gamma$, where γ is the relativistic factor of the electron ($\Delta\tau$ corresponds to the photon formation region, see Ref.[3] for further details). In Supplementary Fig. 6 we show the variation of the average $\langle\eta\rangle$, standard deviation σ_η, minimum $\eta_{\min}$ and maximum $\eta_{\max}$ values of η obtained from a sample of 1024 electrons of the beam initially uniformly distributed in the whole computational box. In Supplementary Fig. 6a we consider the case with initial beam number density $n_b = 3\times10^{18}$ cm^{-3}, i.e. the lowest density case, where the beam-target plasma does not become unstable and the beam energy converted into radiation is modest. In Supplementary Fig. 6b we consider the highest density case $n_b = 6\times10^{20}$ cm^{-3}, where the instability growth rate is the highest and the emission of radiation is the most prominent. In spite of the large differences in the initial beam density, instability growth rate and radiation emission, in both Supplementary Fig. 6a and in Supplementary Fig. 6b we have that $\langle\eta\rangle \lesssim 10^{-5}$, $\sigma_\eta \lesssim 10^{-4}$, $\eta_{\min} \lesssim 10^{-10}$ and $\eta_{\max} \lesssim 10^{-2}$. Thus, the conditions for the applicability of the LCFA are fully satisfied in all the cases considered in our paper.

References

1. XCOM: Photon Cross Sections Database. https://www.nist.gov/pml/xcom-photon-cross-sections-database.
2. Patrignani, C. *et al.* Review of Particle Physics. *Chin. Phys. C* **40**, 100001 (2016).
3. Baier, V. N., Katkov, V. M. & Strakhovenko, V. M. *Electromagnetic Processes at High Energies in Oriented Single Crystals* (World Scientific, 1998).

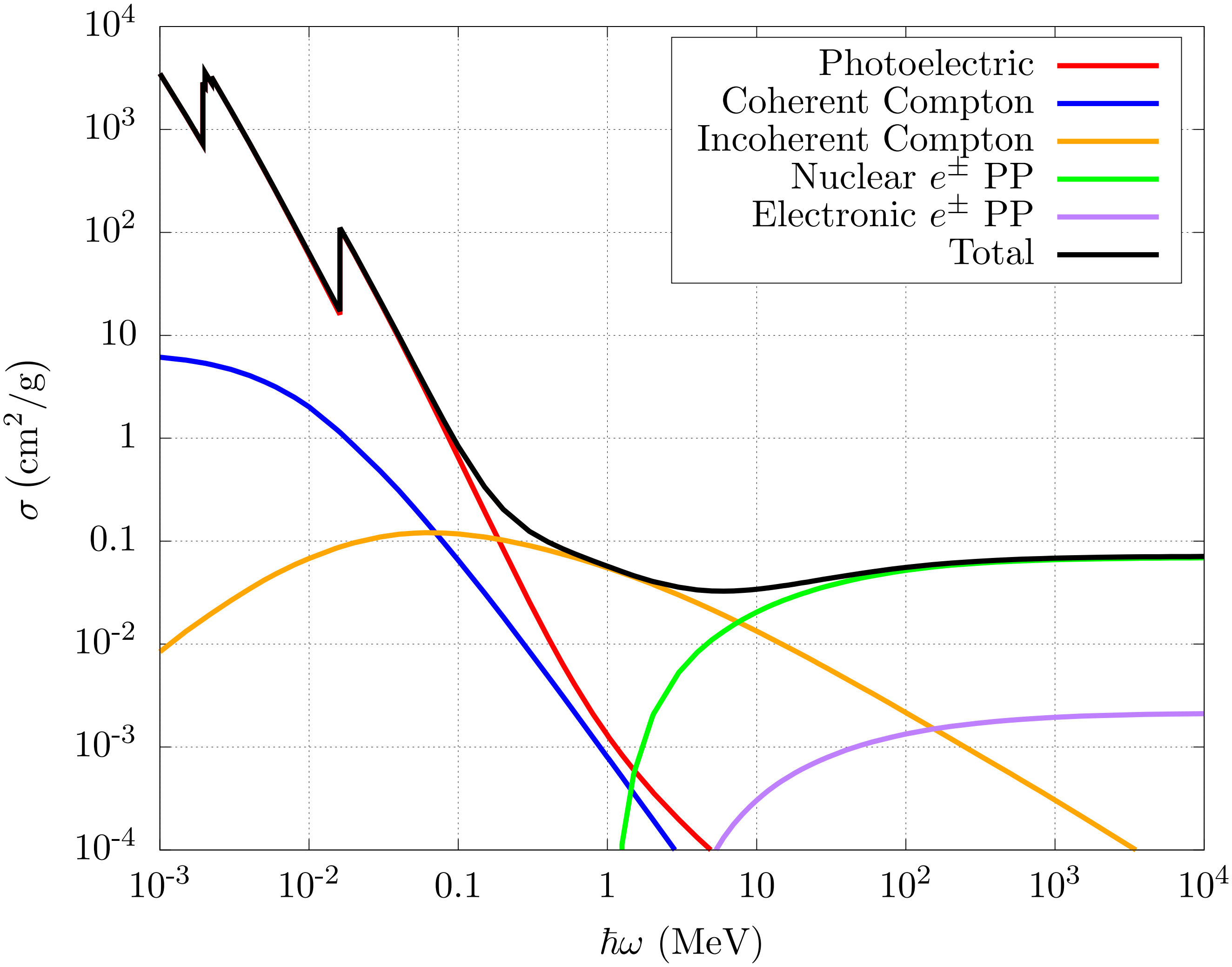

Supplementary Figure 1. **Cross sections**. Photon cross sections as a function of the photon energy in Strontium ($Z = 38$) showing the contributions from the atomic photoelectric effect (electron ejection, photon absorption), coherent (Rayleigh scattering, atom neither ionised nor excited) and incoherent Compton scattering as well as pair production in the nuclear and in the electron fields, respectively. See Refs.[1,2].

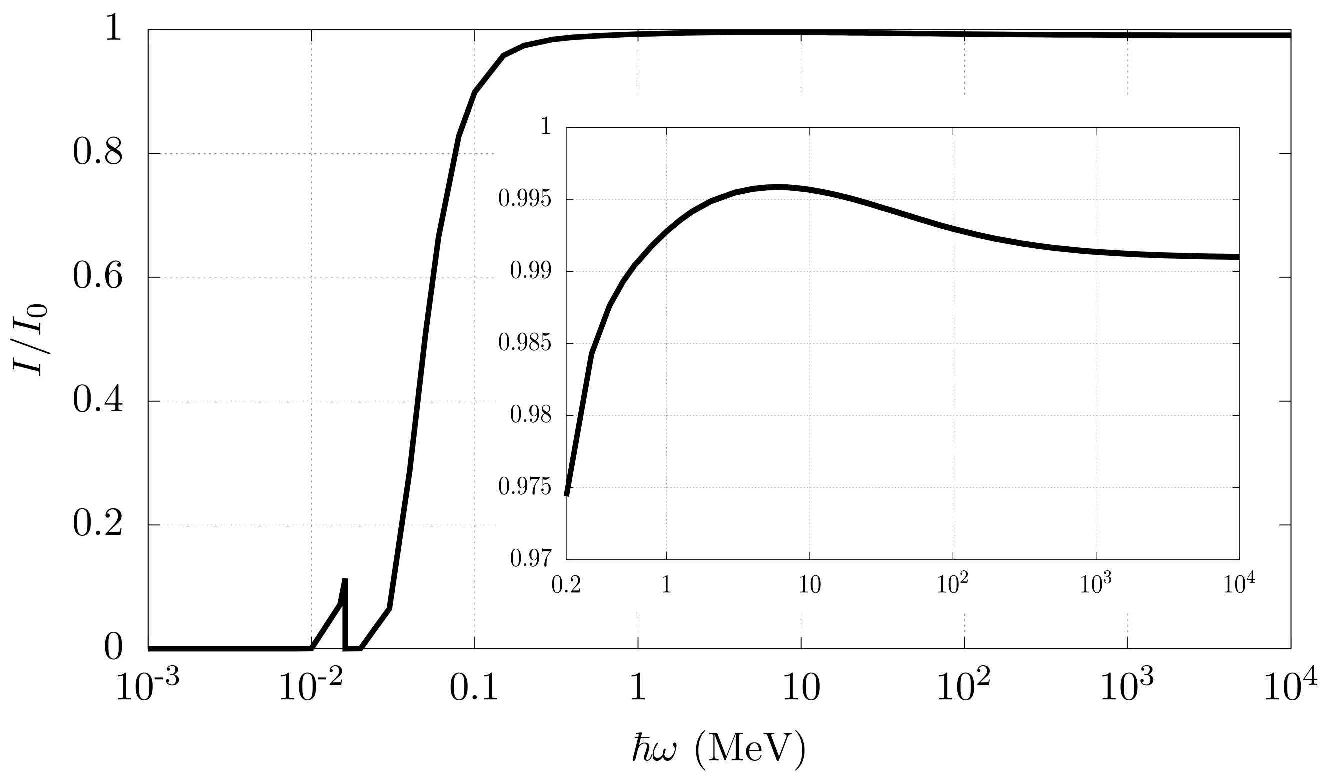

Supplementary Figure 2. Intensity attenuation. Fraction of the photon beam intensity I/I_0 emerging from a metallic Strontium ($Z = 38$) target with thickness $z_{\mathrm{max}} = 0.05$ cm and density $d = 2.54$ g/cm^3 as a function of the photon energy. The inset displays a zoom of the plot in the range $I/I_0 \in [0.97, 1]$ and $\hbar\omega \in [0.2 \text{ MeV}, 10 \text{ GeV}]$.

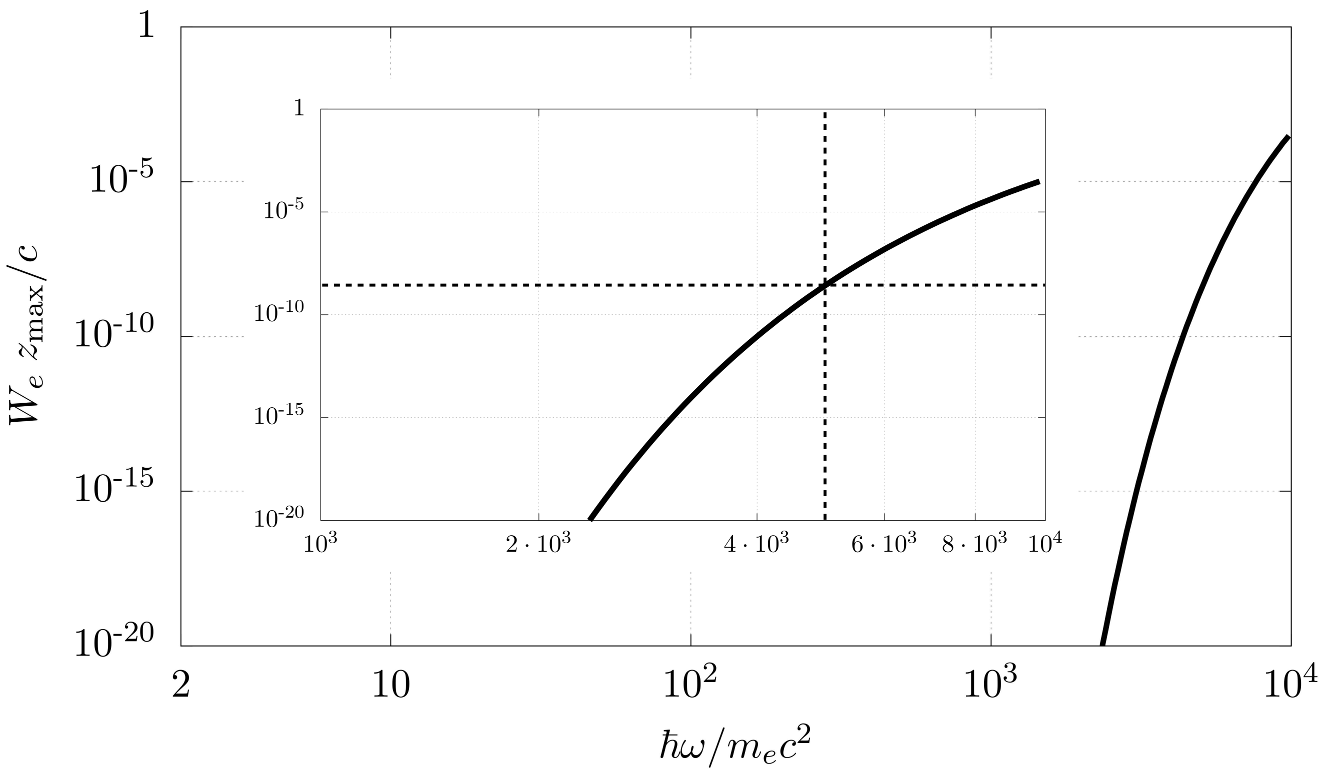

Supplementary Figure 3. Breit-Wheeler pair production. Probability for a single photon with energy $\hbar\omega$ to produce an electron-positron pair when it travels a distance $z_{\text{max}} = 0.05$ cm in the presence of a constant electromagnetic field $F_\perp = 10^9$ esu. The inset displays a zoom of the plot in the range $\hbar\omega \in [10^3, 10^4]\ m_e c^2$. The vertical dashed line corresponds to the maximum photon energy considered in our work $\hbar\omega_{\text{max}} = 2.5$ GeV and the horizontal dashed line highlights the corresponding electron-positron pair production probability of about 10^{-8}.

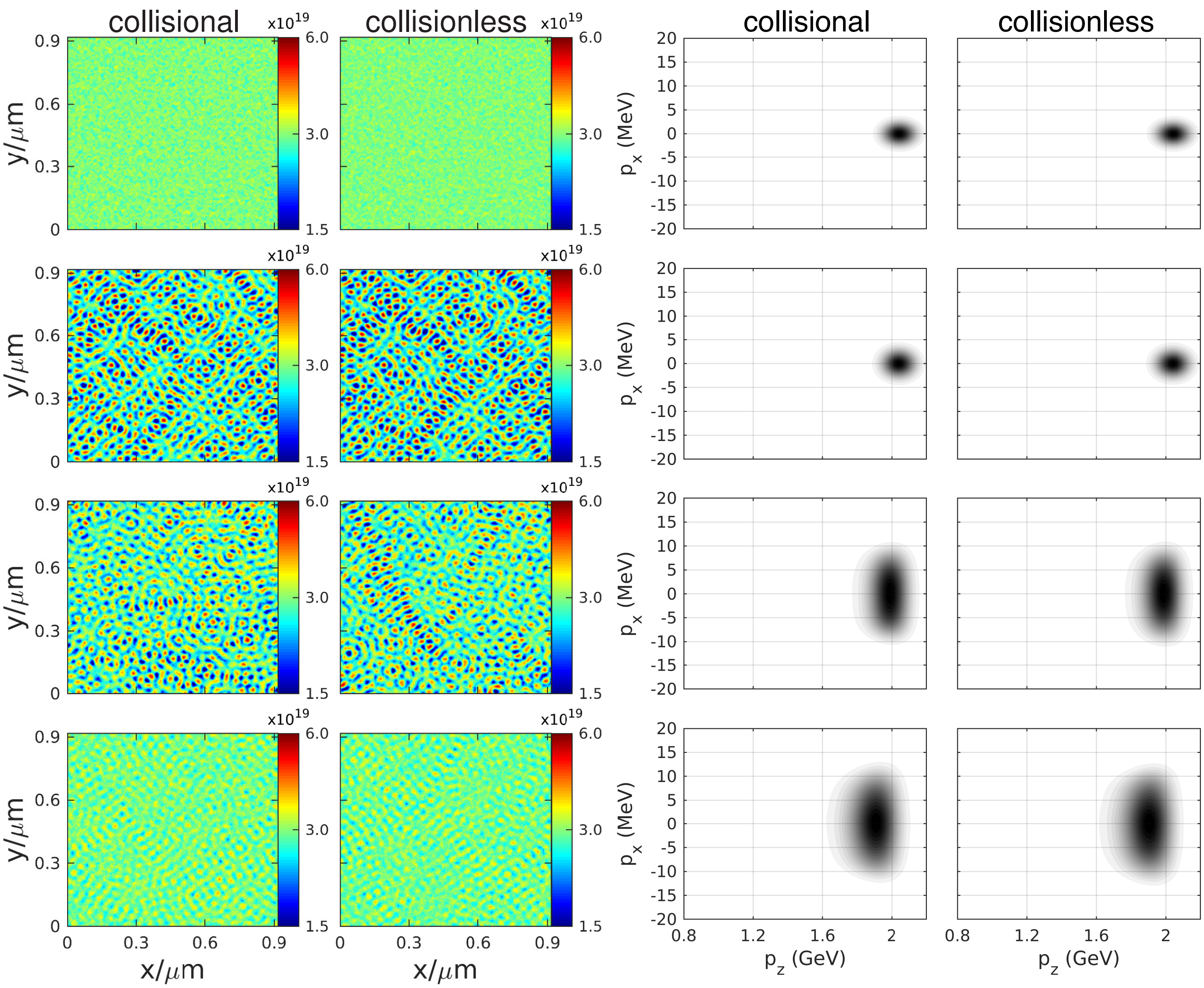

(a) Electron beam number density.

(b) Electron beam momentum distribution.

Supplementary Figure 4. Collisional and collisionless simulation results for $n_b = 3 \times 10^{19}$ cm^{-3}. a, Evolution of the electron beam number density distribution in the plane perpendicular to the beam propagation direction with (left column) and without (right column) collisions. **b**, evolution electron beam momentum distribution in the $p_z p_x$-plane, the electron beam propagating along the z-axis, with (left column) and without (right column) collisions. The plots belonging to the same row report the results obtained when the beam has travelled across the same distance z inside the target. From the top to the bottom: $z = [0.2, 0.8, 2, 3] \times 10^{-2}$ cm.

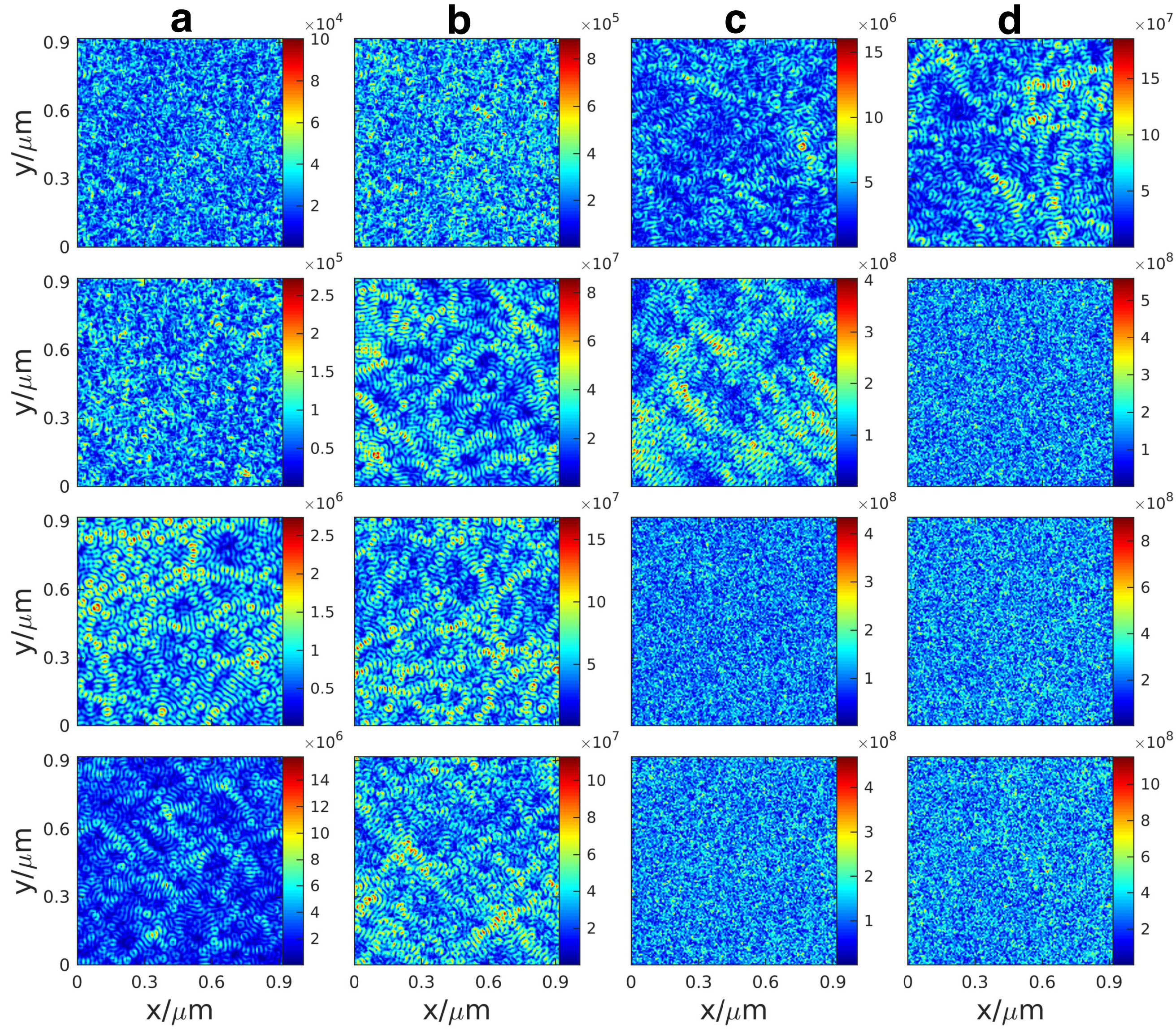

Supplementary Figure 5. **The transverse electromagnetic field**. Evolution of the transverse electromagnetic field $F_\perp$ in the plane perpendicular to the beam propagation direction, which is along the z-axis. The initial electron beam density is: **a**, $n_b = 3\times10^{18}$ cm^{-3}, **b**, 3×10^{19} cm^{-3}, **c**, 2×10^{20} cm^{-3}, **d**, 6×10^{20} cm^{-3}. Snapshots belonging to the same row are taken at the same distance z inside the target. From the top to the bottom: $z = [0.2, 0.8, 2, 3]\times10^{-2}$ cm. The contour plots are obtained from the 3D transverse electromagnetic field distribution by averaging over z the fields in the interval $[z, z+\Delta l_z]$, where $\Delta l_z = 5.75\times10^{-3}$ μm is the spatial resolution. Note the quite different scale of each snapshot due to the large variations of $F_\perp$.

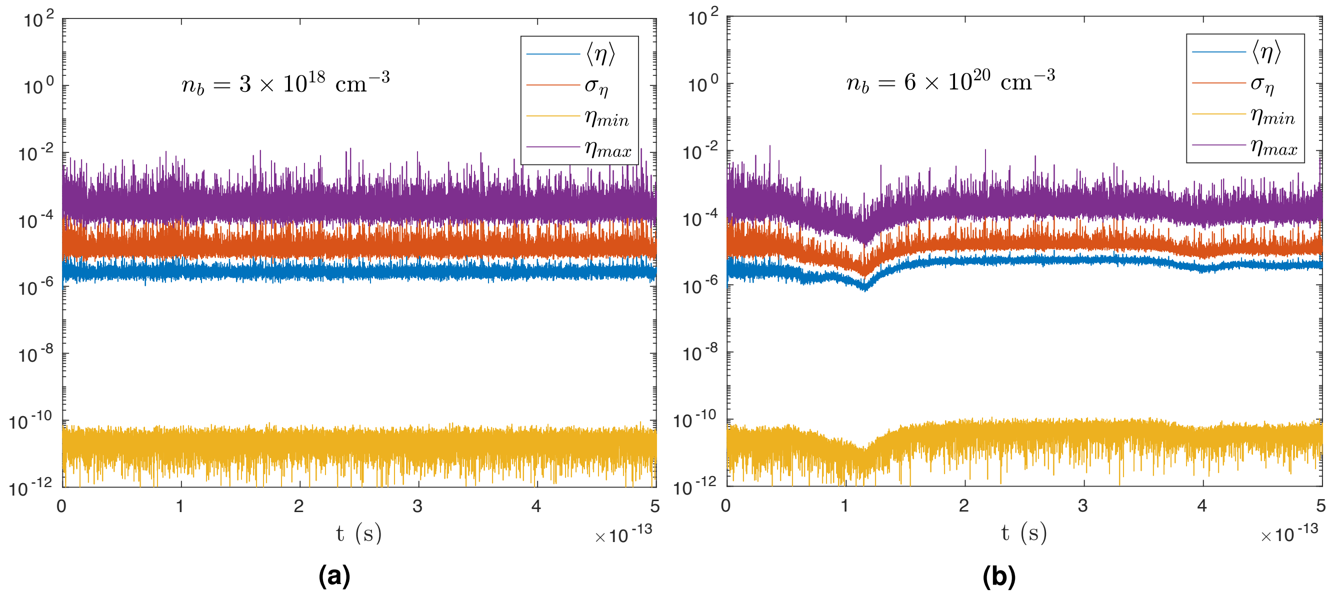

Supplementary Figure 6. Local-constant-field approximation. Evolution of the parameter $\eta = |\dot{F}|\Delta\tau/F$, which provides an estimate of the validity of the LCFA. Here $\langle\eta\rangle$, σ_η, η_{min} and η_{max} are the average, standard deviation, minimum and maximum value of η obtained from a sample of 1024 electrons of the beam initially uniformly distributed in the whole 3D computational box.